energies

MDPI

Article

The Effect of C45 Carbon Black-Phosphomolybdic Acid Nanocomposite on Hydrogenation and Corrosion Resistance of La_2Ni_9Co Hydrogen Storage Alloy

Krystyna Giza [1], Edyta Owczarek [1,*] and Andrzej Miszczyk [2]

[1] Faculty of Production Engineering and Materials Technology, Czestochowa University of Technology, 42-200 Czestochowa, Poland; krystyna.giza@pcz.pl
[2] Chemical Faculty, Gdansk University of Technology, 80-233 Gdansk, Poland; andrzej.miszczyk@pg.edu.pl
* Correspondence: edyta.owczarek@pcz.pl

Abstract: In this paper, we analysed the influence of corrosion processes and the addition of a carbon black-heteropoly phosphomolybdic acid (C45-MPA) nanocomposite on the operating parameters of a hydride electrode obtained on the basis of the intermetallic compound La_2Ni_9Co. The electrochemical properties of negative electrodes for NiMH batteries were studied using galvanostatic charge/discharge curves, the potentiostatic method, and electrochemical impedance spectroscopy (EIS). The morphology and chemical composition analysis of the studied electrodes were investigated by means of scanning electron microscopy (SEM) with supporting energy-dispersive X-ray analysis (EDS). For more structural information, FTIR analysis was performed. The results indicate that the presence of the C45-MPA nanocomposite in the electrode material increased both the discharge capacity of the hydride electrode and the exchange current density of the H_2O/H_2 system. The heteropoly acid-modified electrode is also more resistant to high discharge current densities due to its catalytic activity.

Keywords: MH hydride electrode; phosphomolybdic acid; electrochemical characteristics

Citation: Giza, K.; Owczarek, E.; Miszczyk, A. The Effect of C45 Carbon Black-Phosphomolybdic Acid Nanocomposite on Hydrogenation and Corrosion Resistance of La_2Ni_9Co Hydrogen Storage Alloy. *Energies* **2023**, *16*, 4002. https://doi.org/10.3390/en16104002

Academic Editor: Nikolaos Koukouzas

Received: 18 April 2023
Revised: 5 May 2023
Accepted: 8 May 2023
Published: 10 May 2023

1. Introduction

Hydrogen is undoubtedly one of the energy sources that has grown in popularity in recent years. H_2 is the most abundant and simplest element in the universe. Hydrogen has the highest energy content per unit of weight amongst all the existing energy sources and is non-polluting in nature. Hence, it could be utilized instead of fossil fuels [1–3]. In addition, the great advantage of hydrogen energy compared to other types of energy sources is its ability to be stored and transported. One of the possible methods for hydrogen storage is the application of metal hydride materials [4–8]. Among the many types of metal hydrides, intermetallic AB_5-type alloys have been intensively studied because of their properties, such as fast hydrogen absorption, high reversibility, and proper plateau pressure at room temperature [9–18]. A typical representative of this group of materials, $LaNi_5$-type alloys, are currently used commercially as the negative electrode in NiMH rechargeable batteries [19–21]. Although $LaNi_5$-based hydrogen storage materials have a high-rate discharge capacity, their cycling stability remains unsatisfactory. It is known that, from the practical point of view, one of the basic requirements for the effective operation of hydride cells is the low polarization of the electrodes when drawing significant current from the cell. Such properties are exhibited only by those hydride electrodes that correspond to high exchange current densities. Improving the rate of charging/discharging processes of the hydride electrode is possible, among other methods, by depositing trace amounts of platinum metals (mainly Pt, Rh, Pd, and their alloys) on its surface [22–28]. It should be noted that on the one hand, introducing platinum-group precipitates into the structure of AB_5 alloys accelerates the transport of hydrogen within the hydride phase, but on

the other hand, additions of platinum-group metals to AB_5-type materials may favor the electrochemical degradation of these materials as a consequence of galvanic corrosion. Another effective way to improve the electrochemical activity of the hydride electrode alloy is to increase its surface area, although this leads to an unfavorable reduction in the alloy's resistance to oxidation. An electrode made of an AB_5-type alloy is in direct contact with a strongly alkaline oxidizing electrolyte, which causes the irreversible formation of oxides or hydroxides on its surface [29,30]. From the thermodynamic point of view, it is impossible to avoid the selective oxidation of rare earth elements with a simultaneous reduction in more noble elements (Ni, Co) during charging/discharging processes in a strongly alkaline environment. As indicated in the literature, Keggin-type polyoxometalate (POM), especially heteropoly acids, which improve the kinetics of electrode reactions, may be an alternative to catalysts such as platinum or palladium [31]. Due to such features of polyoxometalates as their well-defined structures and their ability to undergo fast and reversible redox reactions as well as the protection they offer against corrosion, they can be very attractive for energy storage applications [32–36]. Previous electrochemical studies confirmed that after the surface modification of a solid $LaCo_{4.8}Bi_{0.2}$ alloy with phosphotungstic acid (TPA), an increase in the hydrogen absorption efficiency and exchange current density was observed [37]. Bearing in mind that POM, especially phosphododecamolybdic acid $H_3PMo_{12}O_{40}$ (MPA), has the ability to adsorb irreversibly on solid materials such as gold, platinum, and carbon [38–40], we explored the ability of $PMo_{12}O_{40}{}^{3-}$ ions to modify the surface of C45 carbon black particles in order to produce a composite hydride electrode based on the $LaNi_5$ hydrogen storage alloy. Preliminary research results [41,42] indicate that phosphomolybdic acid (MPA) immobilized on the surface of conductive C45 carbon black is stable in a 6 M KOH solution and has electrocatalytic properties. In this study, the powdered active material La_2Ni_9Co was modified with a nanocomposite of carbon black C45-phosphoromolybdic acid (MPA) in order to accelerate the rate of electron transfer across the electrode–solution interface and/or create a protective barrier for the hydride alloy against degradation during repeated hydrogenation/dehydrogenation cycles.

2. Research Material and Methodology

The commercially available La_2Ni_9Co alloy (American Elements, Los Angeles, CA, USA) with a $CaCu_5$-type structure [43], characterized by a reversible ability to absorb hydrogen, was selected for the study. The alloy was ground in a planetary mill (Pulverisette 6 Classic Line Fritsch, Weimar, Germany) in an argon atmosphere and sieved to obtain a powder fraction with a particle size of 20–50 μm.

Composite powder electrodes were prepared by mixing a hydrogen storage material (La_2Ni_9Co alloy) with C45 carbon black and polyvinylidene fluoride (PVDF) in a weight ratio of 85:5:10. The well-mixed components were molded in a laboratory press at 50 bar and dried at 110 °C for an hour. The obtained composite electrodes contained 0.030 ÷ 0.035 g of La_2Ni_9Co alloy.

Modified electrodes were obtained using the same procedure as described above, where the active material (La_2Ni_9Co) in the amount of 85 wt% was mixed with the addition of the C45 carbon black-phosphomolybdic acid (C45-MPA) nanocomposite (5 wt%) and bonded with PVDF (10 wt%).

To produce the C45-MPA nanocomposite, approximately 150 mg of C45 carbon black was dispersed in 10 cm^3 of a 0.04 mol dm^{-3} aqueous solution of $H_3PMo_{12}O_{40}$ (MPA). The suspension was sonicated for 4 h and then centrifuged. The upper liquid layer of the solution was removed and replaced with fresh heteropoly acid solution. The sonication/centrifugation steps were repeated three times, after which the carbon black particles were rinsed with plenty of distilled water (at least 3–4 times) to ensure all excess (non-carbon black) phosphoromolybdenum ions were removed.

The morphology and chemical composition of the C45 carbon black before and after its surface modification with heteropoly acid were examined utilizing a JEOL JSM-6610 LV scanning electron microscope (SEM) coupled with an X-ray energy dispersion spectrometer

(EDS). The surface morphology of the hydride electrodes after chronopotentiometric tests was also assessed by SEM. For more structural information, the characteristics of the carbon black C45, C45-MPA, and MPA were also examined with an Iraffinity-1S FTIR SHIMADZU (Kyoto, Japan) spectrophotometer with an ATR Quest Specac attachment.

DC and AC electrochemical studies were carried out in aerated 6 M KOH, at room temperature, in a three-electrode system (the working electrode—the hydride electrode, the reference electrode—a saturated calomel electrode (SCE), the auxiliary electrode—a platinum electrode in the form of a spiral) using an electrochemical measuring station (CHI Instruments USA, Bee Cave, TX, USA).

3. Research Results

Micrographs of the surface of the C45 carbon black particles before and after chemical modification with $H_3PMo_{12}O_{40}$ acid along with the qualitative EDS microanalysis are shown in Figure 1.

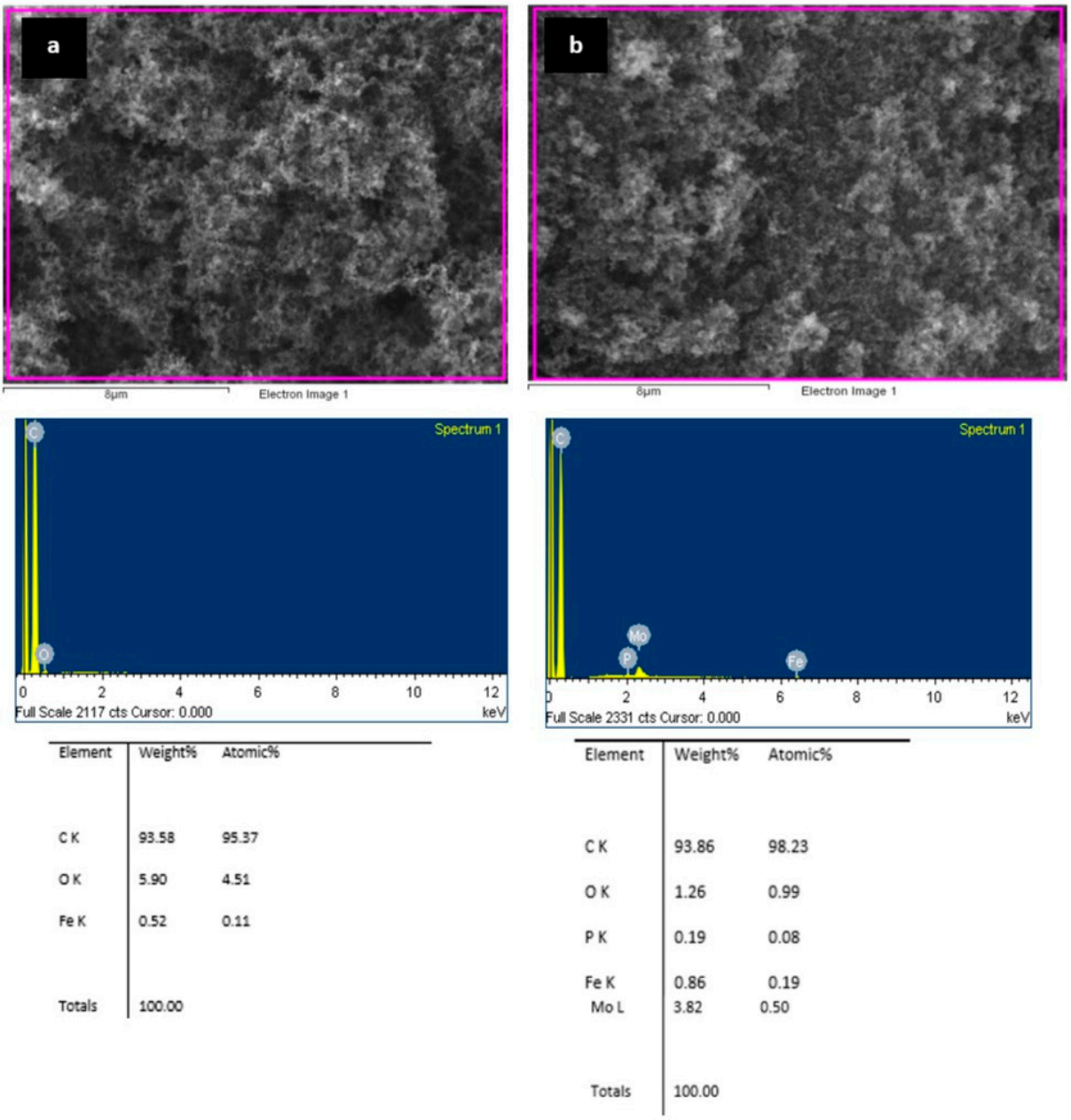

Element	Weight%	Atomic%
C K	93.58	95.37
O K	5.90	4.51
Fe K	0.52	0.11
Totals	100.00	

Element	Weight%	Atomic%
C K	93.86	98.23
O K	1.26	0.99
P K	0.19	0.08
Fe K	0.86	0.19
Mo L	3.82	0.50
Totals	100.00	

Figure 1. Results of SEM–EDX qualitative analysis of C45 carbon black (**a**) and C45-MPA (**b**).

According to the SEM-EDS analysis, the C45 carbon black contained carbon (93.6 wt%) and oxygen (5.9 wt%) and a negligible amount of iron (0.5 wt%), which can be considered as surface contamination. In the modified carbon black C45, next to carbon (93.9 wt%), oxygen (1.3 wt%), and the aforementioned iron, molybdenum (3.8 wt%) was detected the most. Phosphorus was also found in the amount of 0.2% by weight. After modification, carbon black C45 with MPA oxygen content is reduced from 5.9 to 1.26 wt%. It can be assumed that part of the volatile oxygen associated with the C45 carbon black has been partially removed, which may have a beneficial effect on its catalytic properties.

Figure 2 shows FTIR spectra obtained for the carbon black C45 (a), nanocomposite C45-MPA (b), and MPA acid (c). For both C45 (a) and C45-MPA (b), the characteristic peaks corresponding to C-H appeared at 1260cm^{-1}, C=C at 1400 cm^{-1}, and C=O at 1739 cm^{-1}. In the pristine MPA (c) acid spectra, the Keggin structure of $PMo_{12}O_{40}{}^{3-}$ characteristic peaks P-O 1068cm^{-1}, Mo=O, 990 cm^{-1}, and Mo-O, 828, 899 cm^{-1} are visible. As for C45-MPA, vibrations of P-O, Mo=O, and Mo-O are observed with a slight shift, confirming the integration of the polyoxometalate with the carbon matrix.

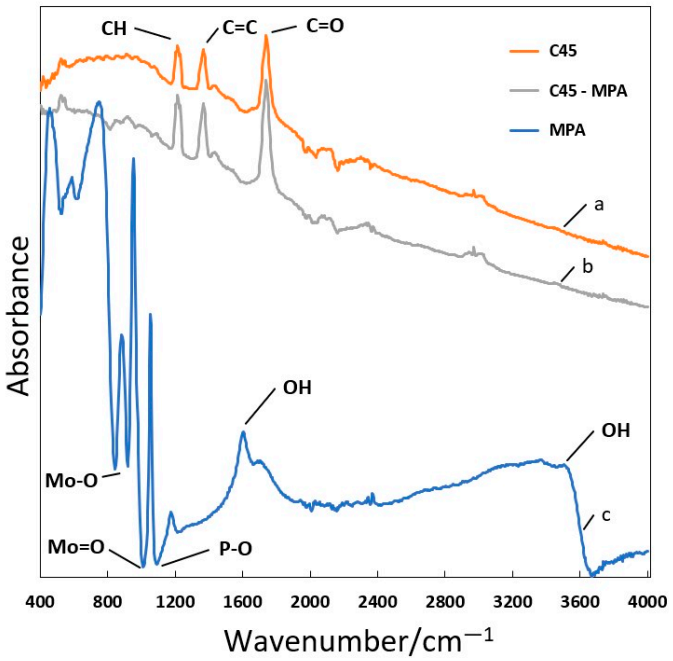

Figure 2. FTIR spectra of C45 carbon black (a), C45-MPA (b), and MPA (c).

Figure 3 displays the course of the cyclic voltammetric (CV) curves of the starting and heteropoly acid-modified electrodes, polarized in the potential range −1.3 V to 0 V (SCE) at the rate of 10 mV s^{-1}. The observed cathode and anodic peaks provide detailed information about the oxidation and reduction processes of the investigated electrodes. As can be seen from Figure 3, for the La_2Ni_9Co alloy modified with heteropoly acid (La_2Ni_9Co-MPA), three oxidation peaks are visible at the potentials of −0.83 V, −0.54 V, and −0.28 V, respectively. The first one at the potential of −0.83 V (SCE) is related to the oxidation of the absorbed hydrogen atoms. It can be seen that the height of the anode current peak for the MPA-modified electrode is slightly higher than that of the heteropoly acid-free starting electrode. The height of the oxidation peak reflects the kinetic properties of the electrode. The higher the anode peak on the voltammetric curve, the greater the electrocatalytic activity of the electrodes [44]. The cathode peak of the reduction of water to hydrogen often expands, which is associated with the evolution of hydrogen on the surface of the hydride electrodes and may not be visible. The other two oxidation peaks visible for the La_2Ni_9Co-MPA electrode at the potentials of −0.54 V and −0.28 V, and the reduction peak at the potential of −0.56 V, can be attributed to the oxidation and reduction in molybdenum within the $PMo^{V}Mo_{11}{}^{VI}O_{40}{}^{4-}$ anion [42,45]. For comparative purposes, Figure 3 additionally shows

the CV for the non-hydrogenated C45-MPA electrode, where two slight oxidation peaks and one reduction peak are also visible at the potentials of −0.50 V, −0.25 V, and −0.48 V, respectively.

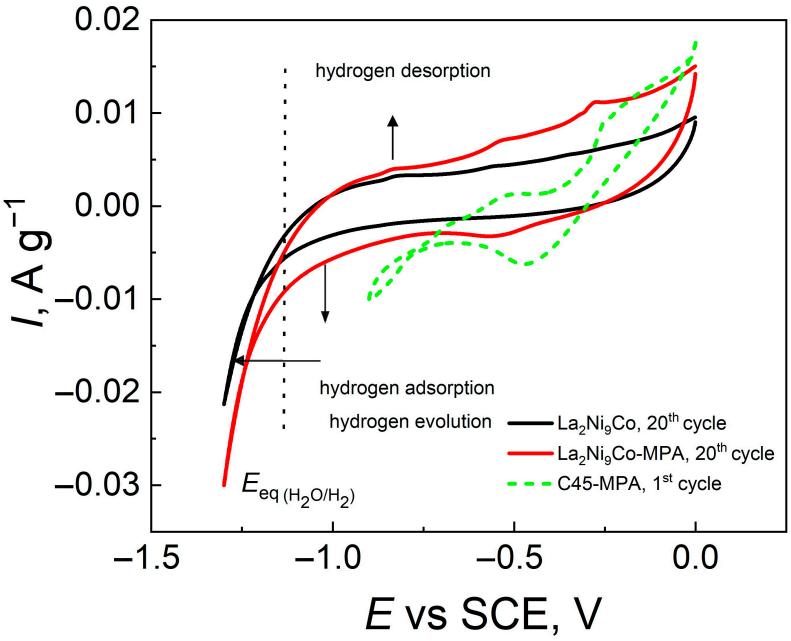

Figure 3. Cyclic voltammograms recorded at scan rate of 10 mV s^{-1}.

Figure 4a presents exemplary charge/discharge curves for the 1st and 10th cycles of two materials: La_2Ni_9Co and La_2Ni_9Co-MPA, and Figure 4b shows the corresponding dependencies of the discharge capacity-cycle number and the exchange current-cycle number resulting from these waveforms. The researched electrodes were saturated with hydrogen for 2.5 h using a constant current density i_{chg} = −185 mA g^{-1}, and then they were discharged at a constant current density i_{dchg} = 50 mA g^{-1}. In addition to the current capacitances, the current densities of the H_2O/H_2 system exchange were determined from the course of the charging and discharging curves on the basis of potential jump ΔE during the switch of cathodic to anode current [14,46]. The discharge capacities of the electrode containing the C45-MPA nanocomposite obtained during the activation process are approximately 38–52 mAh g^{-1} higher than the capacities of the unmodified La_2Ni_9Co. In addition, the exchange current densities for La_2Ni_9Co-MPA, depending on the cycle number, are from approximately 26 to 46% higher than for La_2Ni_9Co.

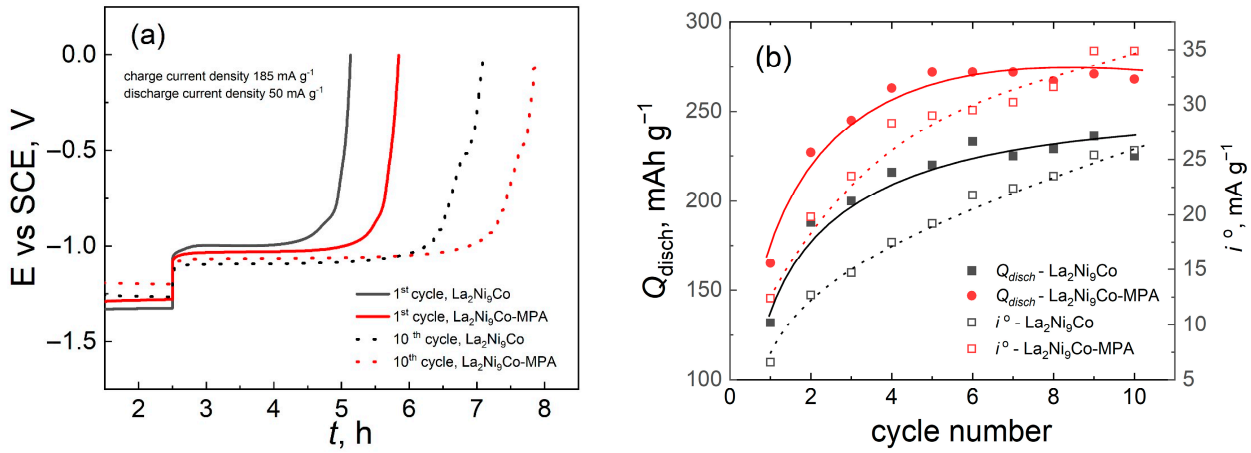

Figure 4. Galvanostatic charge/discharge curves (**a**); discharge capacity and exchange current density as a function of number of cycles (**b**).

The exact effect of the action of phosphomolybdic acid on the absorption/desorption of hydrogen storage alloys has not yet been thoroughly investigated. It can be speculated that its mechanism of action is correlated with better hydrogen adsorption due to the presence of surface groups with a high negative charge. Several papers [31,45,47,48] posit that increasing the charge of the Keggin anion may contribute to its higher catalytic activity. This would favor the accumulation of H_2O dipoles before their reduction according to the following reaction:

$$PMo^{V}Mo_{11}{}^{VI}O_{40}{}^{4-} + ne + nH_2O \rightleftarrows H_nPMo^{V}{}_{1+n}Mo^{VI}{}_{11-n}O_{40}{}^{(4+n)-} + nOH^- \quad (1)$$

leading to an increase in the hydrogen capacity of the heteropoly acid-modified electrode.

Changes in the open circuit potential (OCP) for the examined electrodes as a function of time are shown in Figure 5. The potential was measured against the SCE immediately after the electrodes were immersed in the corrosive solution and after their activation (10 charge/discharge cycles). The OCP measured after the activation process is −1.0 and −1.1 V for the La_2Ni_9Co and La_2Ni_9Co-MPA electrodes, respectively, and is close to the equilibrium potential of the H_2O/H_2 system [49]. The OCP value being higher by 100 mV for the unmodified electrode may be caused by a more intense oxidation of metallic components on the surface of the hydrogen storage material particles. There are many indications that the formation of a tight passive layer leads to selective inhibition of the partial anodic process of the H_2O/H_2 system (oxidation of the residual hydrogen that has not yet diffused from the inside of the particle to the surface)—only then can the equilibrium potential of the hydrogen electrode shift towards positive values. A manifestation of the inhibition of the oxidation of residual hydrogen on the surface of the passivated material is ultimately the shift of the OCP to the anode side, which probably results in significant shortening of the measured discharge time (Figure 4a). The OCP for non-activated electrodes is clearly shifted towards positive potentials and should be treated as the corrosion potential (E_{corr}), describing the corrosion of the material with oxygen depolarization. As can be seen from Figure 5, after 24 h of immersion in the 6 M KOH solution, there is no significant effect of the C45-MPA nanocomposite on the value of the corrosion potential of the La_2Ni_9Co, which is set at −0.33 ÷ −0.35 V versus SCE.

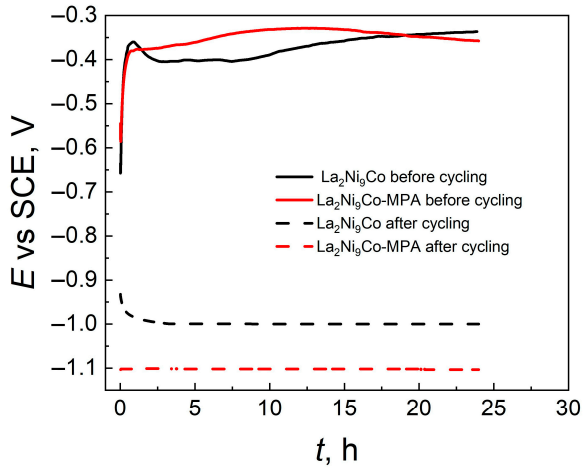

Figure 5. Open circuit potential versus SCE for La_2Ni_9Co and La_2Ni_9Co-MPA electrodes before and after cycling.

Figure 6 displays the potentiokinetic polarization curves of the two electrodes, La_2Ni_9Co and La_2Ni_9Co-MPA, before cycling (solid lines) and after 10 charge/discharge cycles (dashed lines). The employed research methodology (the polarization curves were measured from the potential of −1.3 V with a scanning speed of 1 mV s^{-1}) did not limit the impact of the absorbed hydrogen on the corrosion processes. The course of each polarization curve near the cathode/anode transition reflects the process of hydrogen absorption/desorption

(OCP ≈ −1.0 ÷ −1.1 V), which approximately corresponds to the value of the equilibrium potential of the H_2O/H_2 system. Thus, by extrapolation of the tangents to the OCP (assuming b_k = 0.12V) the exchange current densities of the H_2O/H_2 system can be determined. The exchange currents of the H_2O/H_2 (i^o) system, found by extrapolation, before and after electrode cycling, respectively, take values from 0.23 mA/g to 5.8 mA/g for La_2Ni_9Co and from 3.5 mA/g to 80.0 mA/g for La_2Ni_9Co-MPA. The approximately 14–15 times higher i^o values obtained for the La_2Ni_9Co-MPA electrode indicate a significant influence of the C45-MPA nanocomposite on the improvement in the kinetics of the charge transfer reaction at the electrode/electrolyte interface. The acceleration of the hydrogen absorption/desorption process taking place on the La_2Ni_9Co-MPA electrode is probably caused by the low overpotential of hydrogen evolution on the C45-MPA particles [41].

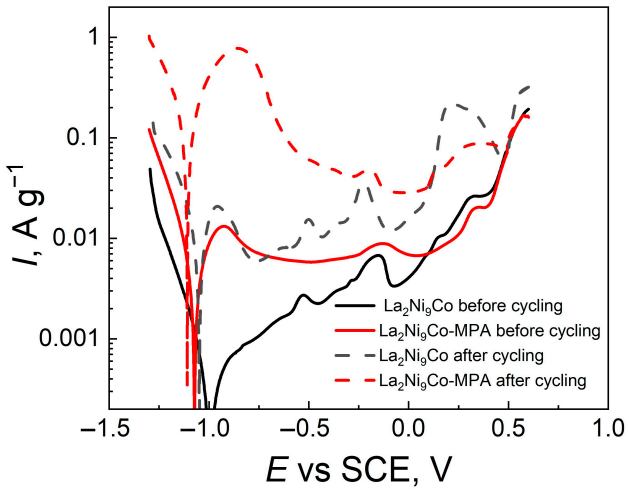

Figure 6. Potentiokinetic curves for La_2Ni_9Co and La_2Ni_9Co-MPA electrodes before and after cycling recorded at scan rate of 1 mV s^{-1}.

The lower currents of the reduction of water molecules to hydrogen for the reference electrode (La_2Ni_9Co) observed in Figure 6 probably result from the progressing corrosion of the material and are an important confirmation that the corrosion phenomena lead to the inhibition of hydrogen absorption processes by hydride alloys. As can be seen from Figure 6, for the non-activated La_2Ni_9Co electrode, an increasing course of anode currents in the passive range is observed, and for La_2Ni_9Co-MPA, a clear anode peak at the potential of −0.93 V indicates the oxidation of hydrogen absorbed during cathodic polarization. One should be aware that at the potentials of −0.95 ÷ −0.76 V, apart from the processes of oxidation of metallic components typical for corrosion, hydrogen absorbed in the cathodic range is also oxidized. When analysing the anode curves, the presence of two characteristic peaks at E = −0.53 ÷ −0.50 V and E = −0.22 ÷ −0.18 V should be noted. The thermodynamic analysis shows that these peaks may be responsible for nickel oxidation and cobalt (M). In the passive range, as the potential increases, the degree of oxidation of both nickel and cobalt in the oxide phase grows (its composition changes from MO through M_3O_4 to M_2O_3). At higher positive potentials, M_2O_3 is oxidized to MO_2 [50]. For the La_2Ni_9Co-MPA electrode, the anode peak of hydrogen oxidation to water expands with the increase in absorbed hydrogen, causing the peak in the potential range −0.53 ÷ −0.50 V associated with the oxidation of molybdenum within the anion $PMo^{V}Mo_{11}{}^{VI}O_{40}{}^{4-}$, which may not be visible.

Figure 7 shows the effect of the discharge rate on both the measured capacity of the investigated electrodes and the exchange current density. Especially at the higher discharge rate (500 mA·g^{-1}) for the La_2Ni_9Co-MPA electrode, a slower decrease in both the capacity and the exchange current density is visible. In the case of the unmodified electrode, a much larger part of hydrogen, at high discharge rates, cannot keep up with diffusion to the surface and remains in the deeper layers of the electrode material. It is probable that

the more intense oxidation of the surface of the unmodified electrode limits the contact surface between the alloy particles and hinders the rate of hydrogen transport from the depth of the electrode to its surface as well as limiting its penetration from the surface into the depth of the electrode. The modification of the electrode with C45-MPA clearly improves the kinetics of the electron transfer reaction at the electrode/electrolyte interface. The results presented in the papers [51,52] for the modified $La_2Ni_9CoM_x$ (M = Al, Sn, Zn) hydride materials indicate that the exchange current densities of the H_2O/H_2 system for these materials are lower compared to La_2Ni_9Co.

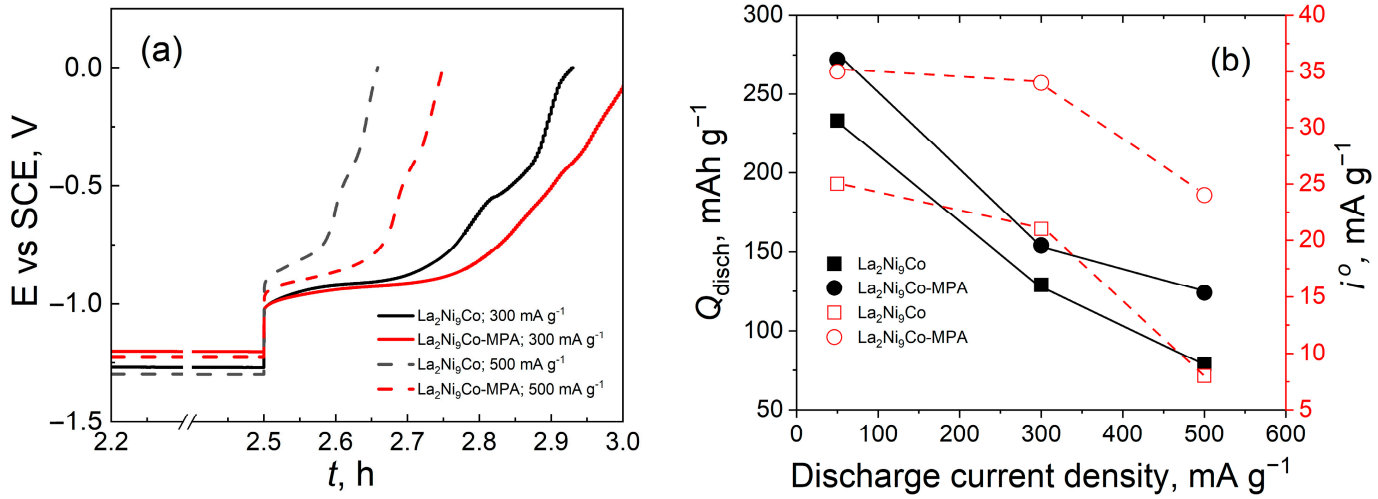

Figure 7. Galvanostatic charge/discharge curves (**a**); discharge capacity and exchange current density as a function of discharge current density (**b**).

As can be seen from Figure 8, after the activation process, the grain of the hydrogen storage alloy powder is characterized by a large number of cracks, but the average particle size of the La_2Ni_9Co alloy is definitely smaller in the case of the electrode modified with the C45-MPA nanocomposite. Thus, this electrode has a larger active surface than the unmodified electrode. The more developed surface of the La_2Ni_9Co-MPA electrode contributes to the increase in the exchange current density of the H_2O/H_2 system. By analysing the elemental composition of the studied powder electrodes (Figure 8), the presence of molybdenum and twice as much carbon and four times less oxygen was confirmed on the surface of the alloy particles modified with the C45-MPA nanocomposite than in the case of the unmodified electrode. Enrichment of the surface of the La_2Ni_9Co alloy particles in C45-MPA delays the process of their oxidation and the formation of tight passive layers, which become a barrier to hydrogen penetration and an increase in the hydrogen capacity. These observations agree very well with the results of the electrochemical tests indicating higher capacitances of the La_2Ni_9Co-MPA electrode in relation to the La_2Ni_9Co electrode at different discharge rates.

Figure 9 presents the Nyquist spectra for the powder electrodes based on the unmodified La_2Ni_9Co alloy and modified with the C45-MPA nanocomposite, obtained at open-circuit potentials after 24 h of immersion of the electrodes in 6 M KOH. The inclination of spectral fragments (an angle less than 90° in relation to the horizontal axis) proves that the surface of the electrodes is inhomogeneous and porous [53]. The observed waveforms are characteristic of porous electrodes with a fractal structure [54]. Figure 10 shows schematically the impedance spectra in the Nyquist system for electrodes without the Faraday reaction described by the de Levie model [55] with the same pores (a), with different pores (b) [56], and the impedance spectrum taking into account fractal type porosity [53,57]. This can be presented schematically as in Figure 10c.

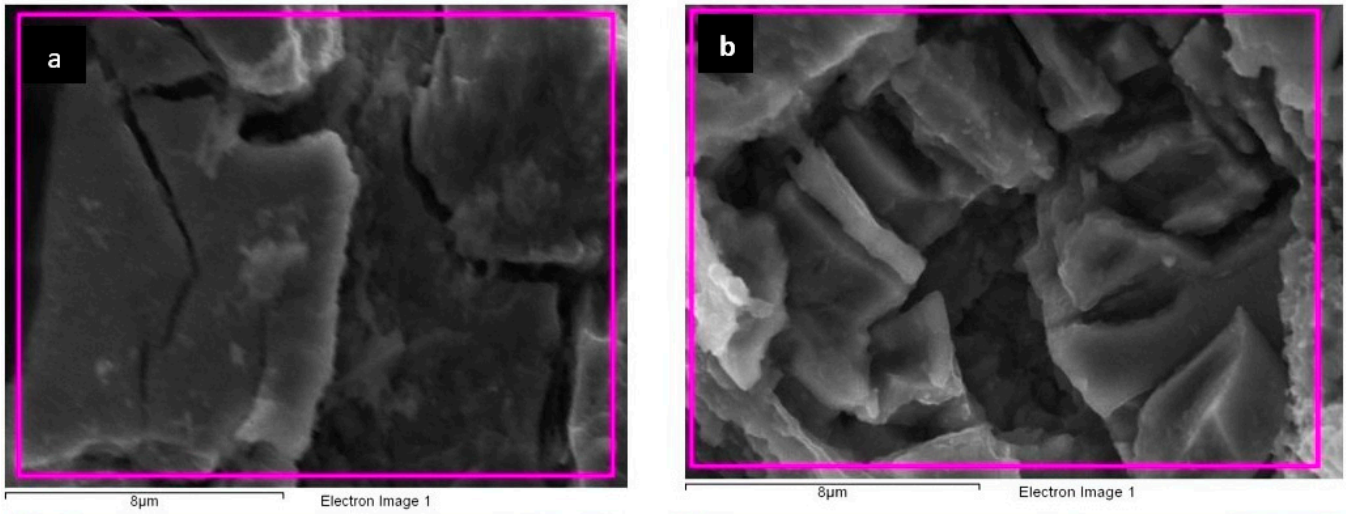

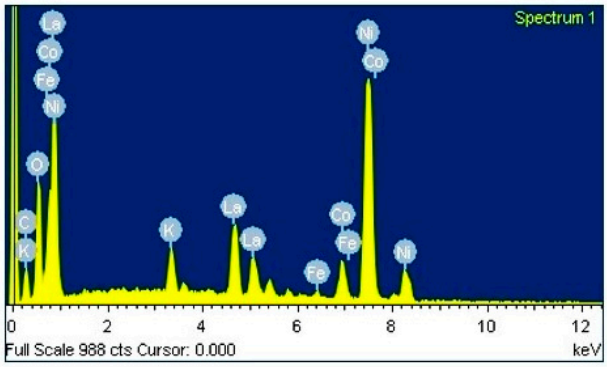

Element	Weight%	Atomic%
C K	6.56	21.98
O K	11.17	28.08
K K	2.63	2.70
Fe K	0.68	0.49
Co K	6.78	4.62
Ni K	53.67	36.77
La L	18.51	5.36
Totals	100.00	

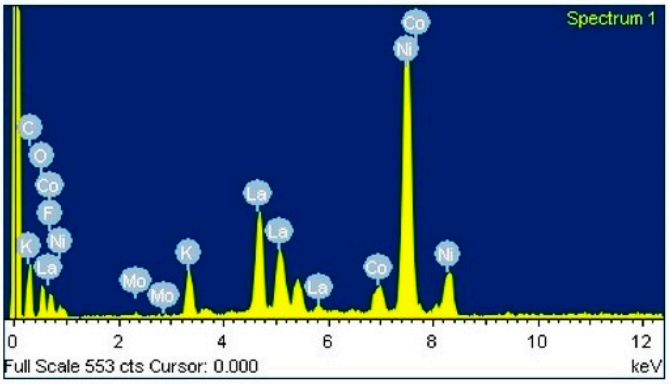

Element	Weight%	Atomic%
C K	12.50	40.83
O K	2.71	6.65
F K	2.45	5.06
K K	2.00	2.01
Co K	4.67	3.11
Ni K	54.20	36.23
Mo L	0.29	0.12
La L	21.17	5.98
Totals	100.00	

Figure 8. SEM micrographs of La_2Ni_9Co (**a**) and La_2Ni_9Co-MPA (**b**) composite electrodes after activation and results of EDS analysis.

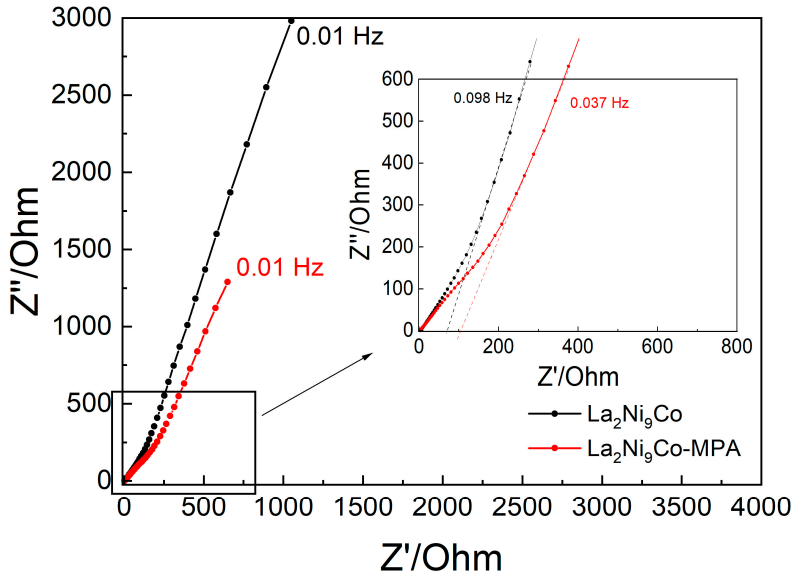

Figure 9. Impedance spectra measured for studied electrodes after 24 h of immersion in 6 M KOH solution. Experimental data: 6 M KOH, 25 °C, frequency range: 100 kHz to 0.01 Hz, amplitude: 5 mV.

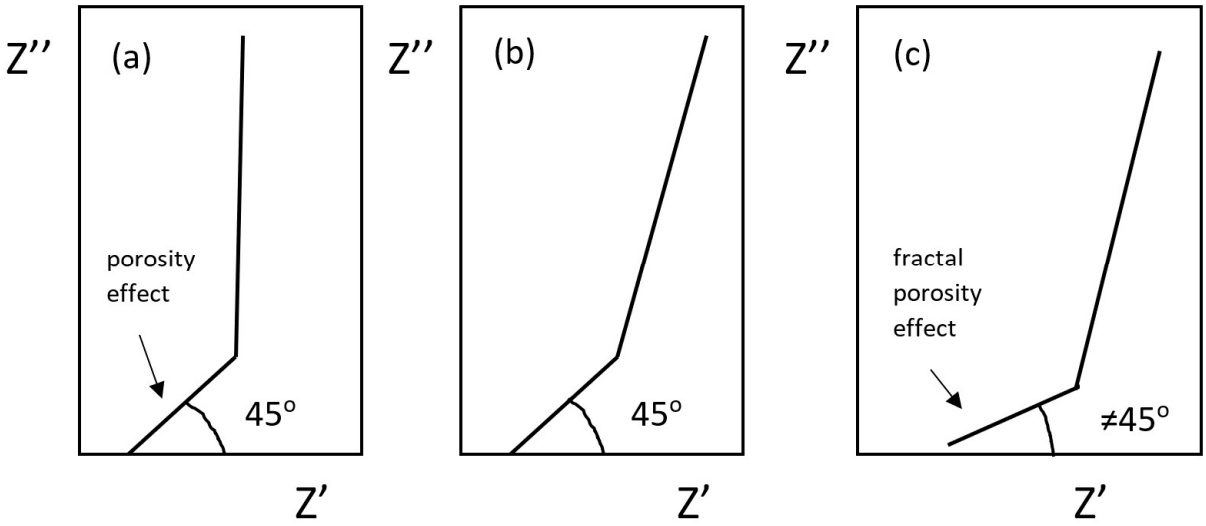

Figure 10. Schematic impedance spectra of porous electrode in Nyquist format according to de Levie with same pores (**a**), with distribution of pore dimensions (**b**), and with fractal pores (**c**).

After modification with the heteropoly acid, the angle of inclination to the horizontal axis decreases, which proves the deepening of the surface heterogeneity through additional inclusions (C45-MPA nanocomposite) or cracking, or the formation of gaps. In Figure 9, displaying the enlarged part of the spectrum, it can be seen that a cracked layer most likely formed on the surface, but at the same time the impedance modulus decreased, which indicates an increase in the active surface available for the electrolyte. This is also evidenced by the shift of the high-frequency part of the spectra (enlarged fragment in Figure 9) along the axis of the real impedance, depicted by dashed lines. For the modified electrode, we observe the appearance of additional resistance, which is responsible for the resistance of the electrolyte in the resulting pores. The larger contact area between the active material and the electrolyte facilitates the rate of H_2O and H_{ads} transport, increasing the activity of the electrode surface for hydrogen absorption/desorption reactions. It can be schematically presented in the form of Figure 11 using the concept of primary porosities characteristic of the unmodified electrode and the appearance of secondary porosities as a result of its modification with the C45-MPA nanocomposite [58].

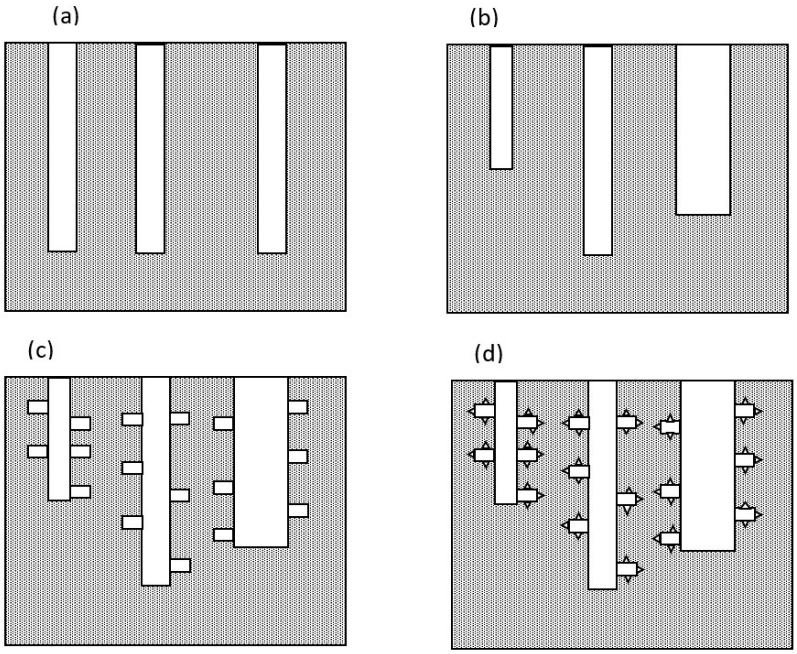

Figure 11. Schematic diagram of electrode with same example pores (**a**), distribution of pores (**b**), fractal pores with primary level of porosity (**c**), and fractal pores with primary and secondary levels of porosity (**d**).

Figure 12 shows the EIS of the electrodes obtained at open-circuit potentials after 10 charge/discharge cycles. As can be seen from Figure 12, the semicircle in the mid-frequency part of the spectrum is distorted at the beginning in the form of a straight line, which proves the well-developed surface of the researched electrodes and their porosity. Gradually, for lower frequencies, it turns into a simple semicircle. The charge transfer resistance is lower for the modified electrode, and the electrochemical reaction proceeds faster, as evidenced by the frequency value at the top of the distorted semicircle. Increasing the surface area of the modified electrode as a result of hydrogen absorption/desorption processes (Figure 8) does not lead to unfavorable chemical degradation of the electrode (does not contribute to an increase in its degree of oxidation), and the C45-MPA nanocomposite can be a bridge that connects adjacent alloy particles, reducing both their contact resistance and charge transfer resistance.

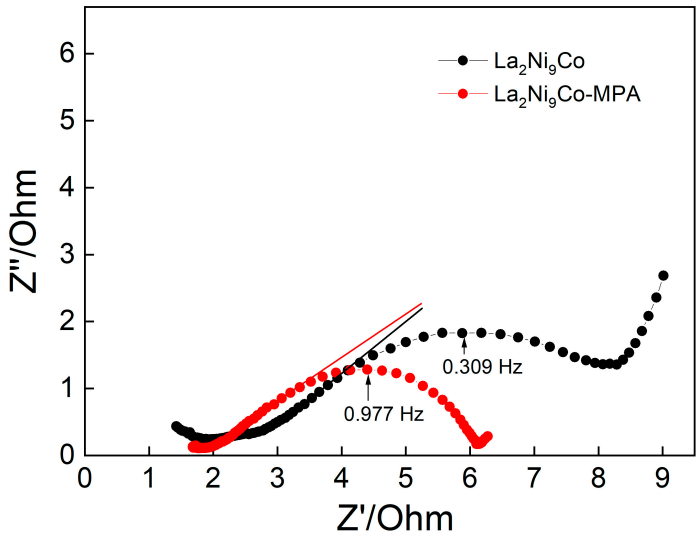

Figure 12. Impedance spectra measured for studied electrodes after ten charge/discharge cycles. Experimental data: 6 M KOH, 25 °C, frequency range: 100 kHz to 0.01 Hz, amplitude: 5 mV.

4. Conclusions

- FTIR analysis of the C45 carbon black conducted before and after the chemical modification confirmed the integration of the Keggin structure of the $PMo_{12}O_{40}^{3-}$ anion with the carbon matrix in the C45-MPA nanocomposite.
- The addition of the C45-MPA carbon black nanocomposite leads to better capacitive and kinetic parameters of the studied composite hydride electrodes.
- The presence of a conductive C45-PVDF matrix and mixed Mo(VI,V) valence sites facilitates electron transfer and charge accumulation.
- The OCP values and the EDS analysis of the electrode surface after the charging/discharging processes indicate that the unmodified electrode oxidizes much more strongly, and the C45-MPA nanocomposite can be a protective barrier for the La_2Ni_9Co alloy against chemical degradation.
- Higher anode currents in the passive range of the modified electrodes are the result of their much larger effective surface in relation to the active surface of the reference and their greater hydrogen capacity.
- The use of $H_3PMo_{12}O_{40}$ may be important in the design of new anode materials for NiMH batteries, but further work is needed to optimize the composition of the C45-MPA nanocomposite.

Author Contributions: Conceptualization, K.G. and E.O.; methodology, K.G. and E.O.; validation, K.G. and E.O.; formal analysis, K.G., E.O. and A.M.; investigation, K.G. and E.O.; writing—original draft preparation, K.G, E.O. and A.M.; writing—review and editing, K.G., E.O. and A.M.; visualization, K.G. and E.O. All authors have read and agreed to the published version of the manuscript.

Funding: The work was supported by statutory research (BS/BP-200-301/2023) funds from the Faculty of Production Engineering and Materials Technology, Czestochowa University of Technology, Poland.

Data Availability Statement: The data presented in this study are available on request from the corresponding author.

Conflicts of Interest: The authors declare no conflict of interest. The funders had no role in the design of the study; in the collection, analyses, or interpretation of data; in the writing of the manuscript; or in the decision to publish the results.

References

1. Baykara, S.Z. Hydrogen: A brief overview on its sources, production and environmental impact. *Int. J. Hydrogen Energy* **2018**, *43*, 10605–10614. [CrossRef]
2. Schlapbach, L.; Züttel, A. Hydrogen-storage materials for mobile applications. *Nature* **2001**, *414*, 353–358. [CrossRef] [PubMed]
3. Singh, S.B.; De, M. Scope of doped mesoporous (<10 nm) surfactant-modified alumina templated carbons for hydrogen storage applications. *Int. J. Energy Res.* **2019**, *43*, 4264–4280. [CrossRef]
4. Pasquini, L.; Sakaki, S.; Akiba, E.; Allendorf, M.D.; Cho, Y.W.; Alvares, E.; Ares, J.D.; Badai, D.; Bricco, M.; von Colbe, J.B.; et al. Magnesium- and Intermetallic Alloys-Based Hydrides for Energy Storage: Modelling, Synthesis and Properties. *Prog. Energy* **2022**, *4*, 032007. [CrossRef]
5. Tarasov, B.P.; Fursikov, P.V.; Volodin, A.A.; Bocharnikov, M.S.; Shimkus, Y.Y.; Kashin, A.M.; Lototskyy, M.V. Metal hydride hydrogen storage and compression systems for energy storage technologies. *Int. J. Hydrogen Energy* **2021**, *46*, 13647–13657. [CrossRef]
6. Yartys, V.A.; Lototskyy, M.V.; Linkov, V.; Pasupathi, S.; Davids, M.W.; Tolj, I.; Radica, G.; Denys, R.V.; Eriksen, J.; Taube, K.; et al. HYDRIDE4MOBILITY: An EU HORIZON 2020 project on hydrogen powered fuel cell utility vehicles using metal hydrides in hydrogen storage and refuelling systems. *Int. J. Hydrogen Energy* **2021**, *46*, 35896–35909. [CrossRef]
7. Hirscher, M.; Yartys, V.A.; Baricco, M.; Bellosta von Colbe, J.; Blanchard, D.; Bowman, R.C.; Broom, D.P.; Buckley, C.E.; Chang, F.; Chen, P.; et al. Materials for Hydrogen-Based Energy Storage Past, Recent Progress and Future Outlook. *J. Alloys Compd.* **2020**, *827*, 153548. [CrossRef]
8. Chen, Z.; Ma, Z.; Zheng, J.; Li, X.; Akiba, E.; Li, H.W. Perspectives and challenges of hydrogen storage in solid-state hydrides. *Chin. J. Chem. Eng.* **2021**, *29*, 1–12. [CrossRef]
9. Fukumoto, M.; Nakajima, K.; Takahashi, H. Formation of $LaNi_5$ hydrogen storage alloy by electrodeposition of La using molten salt. *Coatings* **2022**, *12*, 1268. [CrossRef]
10. Todorova, S.; Abrashev, B.; Rangelova, V.; Vassileva, E.; Spassov, T. Effect of low Al content on the electrode performance of $LaNi_{5-x}Al_x$ hydrogen storage alloys. *J. Chem. Technol. Metall.* **2023**, *58*, 200–207.

11. Sato, T.; Saitoh, H.; Utsumi, R.; Ito, J.; Nakahira, Y.; Obana, K.; Takagi, S.; Orimo, S.I. Hydrogen absorption reactions of hydrogen storage alloy $LaNi_5$ under high pressure. *Molecules* **2023**, *28*, 1256. [CrossRef] [PubMed]
12. Giza, K.; Iwasieczko, W.; Pavlyuk, V.V.; Bala, H.; Drulis, H. Thermodynamical properties of La–Ni–T (T = Mg, Bi and Sb) hydrogen storage systems. *J. Power Sources* **2008**, *181*, 38–40. [CrossRef]
13. Todorova, S.; Abrashev, B.; Rangelova, V.; Mihaylov, L.; Vassileva, E.; Petrov, K.; Spassov, T. Hydrogen gas phase and electrochemical hydriding of $LaNi_{5-x}M_x$ (M = Sn, Co, Al) alloys. *Materials* **2020**, *14*, 14. [CrossRef] [PubMed]
14. Giza, K.; Owczarek, E. Electrochemical Hydrogenation and Corrosion Behaviour of $LaNi_{5-x}Ge_x$ (x = 0.3 and 0.6) Alloys. *Energies* **2021**, *14*, 5285. [CrossRef]
15. Giza, K.; Iwasieczko, W.; Pavlyuk, V.V.; Bala, H.; Drulis, H.; Adamczyk, L. Hydrogen absorption and corrosion resistance of $LaNi_{4.8}Al_{0.2}$ and $LaNi_{4.8}Al_{0.1}Li_{0.1}$ alloys. *J. Alloys Compd.* **2007**, *429*, 352–356. [CrossRef]
16. Stetskiv, A.; Rożdżyńska-Kiełbik, B.; Kowalczyk, G.; Prochwicz, W.; Siemion, P.; Pavlyuk, V. The structural and thermal stability; electrochemical hydrogenation and corrosion behaviour of $LaT_{5-x}M_x$ (T = Co, Ni and M = Al, Ge, Li) phases. *Solid State Sci.* **2014**, *38*, 35–41. [CrossRef]
17. Giza, K. Electrochemical studies of $LaNi_{4.3}Co_{0.4}Al_{0.3}$ hydrogen storage alloy. *Intermetallics* **2013**, *34*, 128–131. [CrossRef]
18. Pęska, M.; Dworecka-Wójcik, J.; Płociński, T.; Polański, M. The influence of cerium on the hydrogen storage properties of $La_{1-x}Ce_xNi_5$ Alloys. *Energies* **2020**, *13*, 1437. [CrossRef]
19. Joubert, J.M.; Paul-Boncour, V.; Cuevas, F.; Zhang, J.; Latroche, M. $LaNi_5$ related AB_5 compounds: Structure, properties and applications. *J. Alloys Compd.* **2021**, *862*, 158163. [CrossRef]
20. Ouyang, L.; Huang, J.; Wang, H.; Liu, J.; Zhu, M. Progress of hydrogen storage alloys for Ni-MH rechargeable power batteries in electric vehicles: A review. *Mater. Chem. Phys.* **2017**, *200*, 164–178. [CrossRef]
21. Poblano-Salas, C.A.; Sotelo-Mazón, O.; Henao, J.; Corona-Castuera, J.; Martinez, G.; Casales-Diaz, M.; Porcayo-Calderón, J.; Tathagata, K.; Navarro, M.; Kesarla, M.K. Flame sprayed $LaNi_5$-based mischmetal alloy: Building-up negative electrodes for potential application in Ni-based batteries. *J. Therm. Spray Technol.* **2021**, *30*, 1940–1956. [CrossRef]
22. Hubkowska, K.; Soszko, M.; Krajewski, M.; Czerwiński, A. Enhanced kinetics of hydrogen electrosorption in AB_5 hydrogen storage alloy decorated with Pd nanoparticles. *Electrochem. Commun.* **2019**, *100*, 100–103. [CrossRef]
23. Xie, D. Effect of surface coating on electrochemical properties of rare earth-based AB_5-type hydrogen storage alloys. *Int. J. Electrochem. Sci.* **2016**, *11*, 9153–9163. [CrossRef]
24. Williams, M.; Lototsky, M.; Nechaev, A.; Yartys, V.; Solberg, J.K.; Denys, R.V.; Linkov, V.M. Palladium mixed-metal surface-modified AB_5-type intermetallides enhance hydrogen sorption kinetics. *S. Afr. J. Sci.* **2010**, *106*, 1–6. [CrossRef]
25. Modibane, K.D.; Lototskyy, M.; Davids, M.W.; Williams, M.; Hato, M.J.; Molapo, K.M. Influence of co-milling with palladium black on hydrogen sorption performance and poisoning tolerance of surface modified AB_5-type hydrogen storage alloy. *J. Alloys Compd.* **2018**, *750*, 523–529. [CrossRef]
26. Ambrosio, R.C.; Ticianelli, E.A. Studies on the influence of palladium coatings on the electrochemical and structural properties of a metal hydride alloy. *Surf. Coat. Technol.* **2005**, *197*, 215–222. [CrossRef]
27. Visintin, A.; Castro, E.B.; Real, S.G.; Triaca, W.E.; Wang, C.; Soriaga, M.P. Electrochemical activation and electrocatalytic enhancement of a hydride-forming metal alloy modified with palladium, platinum and nickel. *Electrochim. Acta* **2006**, *51*, 3658–3667. [CrossRef]
28. Prigent, J.; Joubert, J.M.; Gupta, M. Modification of the hydrogenation properties of $LaNi_5$ upon Ni substitution by Rh, Ir, Pt or Au. *J. Alloys Compd.* **2012**, *511*, 95–100. [CrossRef]
29. Karwowska, M.; Fijalkowski, K.J.; Czerwiński, A. Corrosion of hydrogen storage metal alloy LaMm-Ni4.1Al0.3Mn0.4Co0.45 in the aqueous solutions of alkali metal hydroxides. *Materials* **2018**, *11*, 2423. [CrossRef]
30. Giza, K.; Owczarek, E. Microstructure and corrosion resistance of $LaNi_{5-x}Mg_x$ alloys. *Micromachines* **2022**, *13*, 1192. [CrossRef]
31. Zhang, Y.; Liu, J.; Li, S.L.; Su, Z.M.; Lan, Y.Q. Polyoxometalate-based materials for sustainable and clean energy conversion and storage. *EnergyChem* **2019**, *1*, 100021. [CrossRef]
32. Genovese, M.; Foong, Y.W.; Lian, K. Designing polyoxometalate based layer-by-layer thin films on carbon nanomaterials for pseudocapacitive electrodes. *J. Electrochem. Soc.* **2015**, *162*, A5041. [CrossRef]
33. Skunik, M.; Chojak, M.; Rutkowska, I.A.; Kulesza, P.J. Improved capacitance characteristics during electrochemical charging of carbon nanotubes modified with polyoxometallate monolayers. *Electrochim. Acta* **2008**, *53*, 3862–3869. [CrossRef]
34. Horn, M.R.; Singh, A.; Alomari, S.; Goberna-Ferrón, S.; Benages-Vilau, R.; Chodankar, N.; Motta, N.; Ostrikov, K.; MacLeod, J.; Sonar, P.; et al. Polyoxometalates (POMs): From electroactive clusters to energy materials. *Energy Environ. Sci.* **2021**, *14*, 1652–1700. [CrossRef]
35. Cuentas-Gallegos, A.K.; Martínez-Rosales, R.; Baibarac, M.; Gomez-Romero, P.; Rincon, M.E. Electrochemical supercapacitors based on novel hybrid materials made of carbon nanotubes and polyoxometalates. *Electrochem. Commun.* **2007**, *9*, 2088–2092. [CrossRef]
36. Bonastre, J.; Garcés, P.; Huerta, F.; Quijada, C.; Andión, L.G.; Cases, F. Electrochemical study of polypyrrole/PW12O403-coatings on carbon steel electrodes as protection against corrosion in chloride aqueous solutions. *Corros. Sci.* **2006**, *48*, 1122–1136. [CrossRef]
37. Giza, K.; Adamczyk, L. Influence of $H_3PW_{12}O_{40}$ on electrochemical properties of $LaCo_{4.8}Bi_{0.2}$ alloy. *Cent. Eur. J. Chem.* **2013**, *11*, 330–334. [CrossRef]

38. Ernst, A.Z.; Zoladek, S.; Wiaderek, K.; Cox, J.A.; Kolary-Zurowska, A.; Miecznikowski, K.; Kulesza, P.J. Network films of conducting polymer-linked polyoxometalate-modified gold nanoparticles: Preparation and electrochemical characterization. *Electrochim. Acta* **2008**, *53*, 3924–3931. [CrossRef]
39. Karnicka, K.; Chojak, M.; Miecznikowski, K.; Skunik, M.; Baranowska, B.; Kolary, A.; Piranska, A.; Palys, B.; Adamczyk, L.; Kulesza, P.J. Polyoxometallates as inorganic templates for electrocatalytic network films of ultra-thin conducting polymers and platinum nanoparticles. *Bioelectrochemistry* **2005**, *66*, 79–87. [CrossRef]
40. Kulesza, P.J.; Skunik, M.; Baranowska, B.; Miecznikowski, K.; Chojak, M.; Karnicka, K.; Ernst, A. Fabrication of network films of conducting polymer-linked polyoxometallate-stabilized carbon nanostructures. *Electrochim. Acta* **2006**, *51*, 2373–2379. [CrossRef]
41. Giza, K. Communication—A New Catalytic Application of $H_3PMo_{12}O_{40}$ in the Performance of Hydride Electrode for Ni-MH Battery. *J. Electrochem. Soc.* **2019**, *166*, A3332–A3334. [CrossRef]
42. Giza, K. Electrochemical characterization of C45 carbon black-$H_3PMo_{12}O_{40}$-polyvinylidene fluoride system. *Ochr. Przed Korozją* **2022**, *65*, 340–343. [CrossRef]
43. Bala, H.; Dymek, M.; Drulis, H. Development of metal hydride material efficient surface in conditions of galvanostatic charge/discharge cycling. *Mat. Chem. Phys.* **2014**, *148*, 1008–1012. [CrossRef]
44. Rozdzynska-Kielbik, B.; Stetskiv, I.; Pavlyuk, V.; Stetskiv, A. Significant improvement of electrochemical hydrogenation, corrosion protection and thermal stability of $LaNi_{4.6}Zn_{0.4-x}Li_x$ ($x \leq 0.2$) solid solution phases due to Li-doping. *Solid State Sci.* **2021**, *113*, 106552. [CrossRef]
45. Maksimovskaya, R. Molybdophosphate heteropoly blues: Electron-transfer reactions in aqueous solutions as studied by NMR. *Polyhedron* **2013**, *65*, 54–59. [CrossRef]
46. Giza, K.; Musiał-Gładysz, A. Evaluation of the influence of Cu_2O addition on electrochemical properties of $LaNi_5$ hydrogen storage alloy. *Ochr. Przed Korozją* **2018**, *61*, 114–118. [CrossRef]
47. Gumerova, N.I.; Rompel, A. Synthesis, structures and applications of electron-rich polyoxometalates. *Nat. Rev. Chem.* **2018**, *2*, 0112. [CrossRef]
48. Kulesza, P.J.; Pieta, I.S.; Rutkowska, I.A.; Wadas, A.; Marks, D.; Klak, K.; Stobinski, L.; Cox, J.A. Electrocatalytic oxidation of small organic molecules in acid medium: Enhancement of activity of noble metal nanoparticles and their alloys by supporting or modifying them with metal oxides. *Electrochim. Acta* **2013**, *110*, 474–483. [CrossRef]
49. Giza, K. Electrochemical properties of $LaNi_{4.2}Co_{0.4}Zn_{0.1}Al_{0.3}$ and $LaNi_{4.3}Co_{0.4}Zn_{0.1}Al_{0.2}$ alloys as anode materials for Ni-MH batteries. *Mater. Test.* **2017**, *59*, 598–601. [CrossRef]
50. Pourbaix, M. *Atlas of Electrochemical Equilibria in Aqueous Solutions*; Pergamon Press: Oxford, UK, 1996.
51. Dymek, M.; Bala, H.; Drulis, H.; Hackemer, A. Hydrogenation and corrosion properties of $LaNi_{4.5}Co_{0.5}$-based alloy doped with 1.7 at% Sn. *Solid State Phenom.* **2015**, *227*, 263–266. [CrossRef]
52. Bala, H.; Gęga, J.; Dymek, M.; Pawlik, P. Activation of superstoichiometric hydride alloy by its selective leaching in 6 M KOH solution. *Ochr. Przed Koroz.* **2019**, *62*, 124.
53. Ogihara, N.; Itou, Y.; Sasaki, T.; Takeuchi, Y. Impedance spectroscopy characterization of porous electrodes under different electrode thickness using a symmetric cell for high-performance lithium-ion batteries. *J. Phys. Chem. C* **2015**, *119*, 4612–4619. [CrossRef]
54. Itagaki, M.; Hatada, Y.; Shitanda, I.; Watanabe, K. Complex impedance spectra of porous electrode with fractal structure. *Electrochim. Acta* **2010**, *55*, 6255–6262. [CrossRef]
55. De Levie, R. On porous electrodes in electrolyte solutions. *Electrochim. Acta* **1963**, *8*, 751–780. [CrossRef]
56. Song, H.K.; Hwang, H.Y.; Lee, K.H.; Dao, L.H. The effect of pore distribution on the frequency dispersion of porous electrodes. *Electrochim. Acta* **2000**, *45*, 2241–2257. [CrossRef]
57. Cericola, D.; Spahr, M.E. Impedance spectroscopic studies of the porous structure of electrodes containing graphite materials with different particle size and shape. *Electrochim. Acta* **2016**, *191*, 558–566. [CrossRef]
58. Gourbeyre, Y.; Tribollet, B.; Dagbert, C.; Hyspecka, L. A physical model for anticorrosion behaviour of duplex coatings. *J. Electrochem. Soc.* **2006**, *153*, B162–B168. [CrossRef]